

## Bio-inspired flexible joints with passive feathering for robotic fish pectoral fins

This content has been downloaded from IOPscience. Please scroll down to see the full text.

2016 Bioinspir. Biomim. 11 036009

(<http://iopscience.iop.org/1748-3190/11/3/036009>)

View [the table of contents for this issue](#), or go to the [journal homepage](#) for more

### Download details:

This content was downloaded by: sanazbehbahani

IP Address: 35.9.136.184

This content was downloaded on 04/05/2016 at 16:53

Please note that [terms and conditions apply](#).

# Bioinspiration & Biomimetics



## PAPER

# Bio-inspired flexible joints with passive feathering for robotic fish pectoral fins

RECEIVED  
4 January 2016

REVISED  
14 March 2016

ACCEPTED FOR PUBLICATION  
29 March 2016

PUBLISHED  
4 May 2016

Sanaz Bazaz Behbahani and Xiaobo Tan<sup>1</sup>

Smart Microsystems Laboratory, Department of Electrical and Computer Engineering, Michigan State University, East Lansing, MI 48824, USA

<sup>1</sup> Author to whom any correspondence should be addressed.

E-mail: [bazazbeh@msu.edu](mailto:bazazbeh@msu.edu) and [xbtan@msu.edu](mailto:xbtan@msu.edu)

**Keywords:** robotic fish, bio-inspired, pectoral fin, labriform swimming mode, dynamic model, blade element theory, efficiency

## Abstract

In this paper a novel flexible joint is proposed for robotic fish pectoral fins, which enables a swimming behavior emulating the fin motions of many aquatic animals. In particular, the pectoral fin operates primarily in the rowing mode, while undergoing passive feathering during the recovery stroke to reduce hydrodynamic drag on the fin. The latter enables effective locomotion even with symmetric base actuation during power and recovery strokes. A dynamic model is developed to facilitate the understanding and design of the joint, where blade element theory is used to calculate the hydrodynamic forces on the pectoral fins, and the joint is modeled as a paired torsion spring and damper. Experimental results on a robotic fish prototype are presented to illustrate the effectiveness of the joint mechanism, validate the proposed model, and indicate the utility of the proposed model for the optimal design of joint depth and stiffness in achieving the trade-off between swimming speed and mechanical efficiency.

## 1. Introduction

Development of robotic fish has been inspired by unique characteristics of swimming in live fish and other aquatic animals, such as agility, maneuverability, and efficiency [1–16]. Robotic fish change their body shape or flap different fins to generate propulsion [17–25]. According to [26], based on the propulsors that fish use, their locomotion can be divided into two main categories: median/paired fin propulsion, and body/caudal fin propulsion. In this work, we consider the case where a robotic fish oscillates its paired pectoral fins to generate thrust. The pectoral fin propulsion provides good maneuverability and stability for robotic fish [27]. There are some studies dealing with robotic fish propelled by paired pectoral fins. Most of the early investigations employed rigid pectoral fins that were motor-driven to produce different fin motions [28–31]. Several recent studies investigated the impact of flexible pectoral fins on robotic fish performance [32, 33]. In order to generate a net thrust, there are typically two strategies. The first strategy involves the use of multiple actuators for each pectoral fin, to provide combinations of different

degrees of freedom, namely rowing, feathering and flapping, where the axes of rotation are vertical, transverse, and longitudinal, respectively. Although this strategy enables the mimicking of live fish pectoral fin motion, it results in large size and high energy consumption for robotic fish [29, 30]. An alternative actuation strategy is to use a single actuator per fin to maintain the small robot size, but employ different power and recovery stroke speeds to minimize the drag force during the recovery stroke. However, this method tends to significantly slow down the fish in the extended recovery stroke period [33]. This issue was addressed in [34], where the authors proposed a design of a passive joint for the rowing motion, which enables the pectoral fin to sweep back passively (along the same rowing axis) in order to minimize the drag force during the recovery stroke.

In this study, to more precisely mimic drag-based labriform swimming mode of live fish [26], we combine two different pectoral fin motions, rowing and feathering, realized with only a single actuator per fin, as illustrated in figure 1. As discussed in [35, 36], a real fish rarely moves its pectoral fin by an exclusive rowing or feathering movement; instead, it uses a combination of

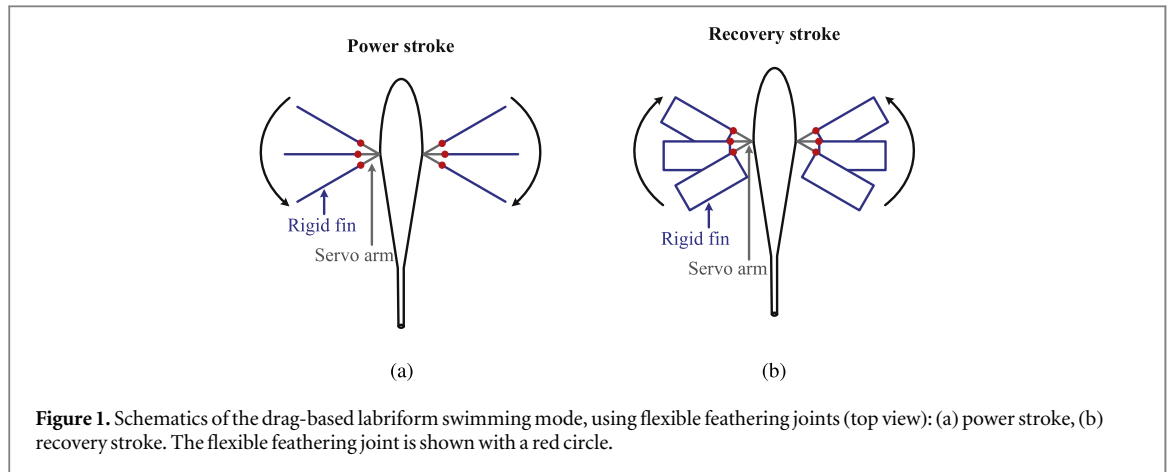


**Figure 1.** Schematics of the drag-based labriform swimming mode, using flexible feathering joints (top view): (a) power stroke, (b) recovery stroke. The flexible feathering joint is shown with a red circle.

these motions to move forward. The contribution of this paper is the design and modeling of a flexible, passively feathering joint that enables the robotic fish to mimic the drag-based labriform swimming mode. Here, the pectoral fin motion is divided into two phases, namely, power and recovery strokes. During the power stroke, the mechanical stoppers of the designed joints allow the paired fins to move backward with respect to the body, following a prescribed rowing motion. This would induce a drag force opposite to the moving direction of the fins, pointing in the forward direction. In the recovery stroke, the pectoral fin feathers passively while following the actuated rowing motion, which effectively reduces the drag force on the fin. The mechanism of the joints and how the stoppers work in each cycle are described in detail in section 2. The proposed joint reduces the cost and complexity of the fin motion, comparing to adopting an active feathering fin [29, 30].

The dynamic model of the pectoral fin is developed based on blade element theory [19], where the joint is modeled as a pair of torsional spring and damper. With the consideration of the combined rowing and feathering motions, the 3D hydrodynamic forces are captured in the model. The model is then validated by conducting different experiments on a robotic fish. The performance of the robotic fish utilizing the flexible feathering joint is also compared with the case where differential actuation during power/recovery strokes is adopted along with a traditional rigid joint. The effect of the depth and stiffness of the flexible joint is further investigated using the dynamic model, which is also validated with experiments. Finally, the mechanical efficiency of the robotic fish is computed for flexible feathering joints for different spring constants and operating frequencies, which provides insight that is useful in optimizing the joint design and the frequency regime of fin flapping.

A preliminary version of this work was presented at the 2014 ASME Dynamic Systems and Control Conference [37]. The improvement of this paper over [37] includes the following. First, on the experimental side, data reported here were collected with a new robotic fish prototype using an enhanced experimental setup

(for example, robot trajectories were captured and extracted with an OptiTrak system, while in [37] the measurements were conducted manually). Most, if not all, figures involving data in this paper are different from those in [37]. Second, the analysis of mechanical efficiency was not included in [37]. Finally, the writing has been polished throughout the paper. In another line of work by the authors [34, 38], an alternative design of flexible joints for pectoral fins was proposed, where the flexible rowing joint allows the fin to sweep back passively (along the same rowing axis) during the recovery stroke. That work, which does not involve feathering motion, is complementary to the current paper with minimal overlap.

The remainder of this paper is organized as follows. In section 2 the design and prototyping of the proposed flexible joint are described in detail. The dynamic model of the joint along with the model for robotic fish adopting such joints is presented in section 3. In section 4 the experimental setup is described and experimental results are provided along with the simulation results to validate the dynamic model. Section 5 is focused on the effect of joint depth and stiffness. Section 6 addresses the calculation of the mechanical efficiency of the robotic fish adopting the flexible joint. Finally, concluding remarks are provided in section 7.

## 2. Design of flexible feathering joint

This section covers the details of design and prototyping of the flexible feathering joint. As mentioned earlier, each pectoral fin follows a rowing motion prescribed by the servo motor, which actuates the proximal end of the fin symmetrically during the power and recovery strokes. Our primary goal is to minimize the drag force during the recovery stroke, by adding another degree of freedom to the pectoral fin, without utilizing any additional actuator. To accomplish this goal, a flexible feathering joint is designed to enable the pectoral fin feather passively when it is rowed back during the recovery stroke. This mode of

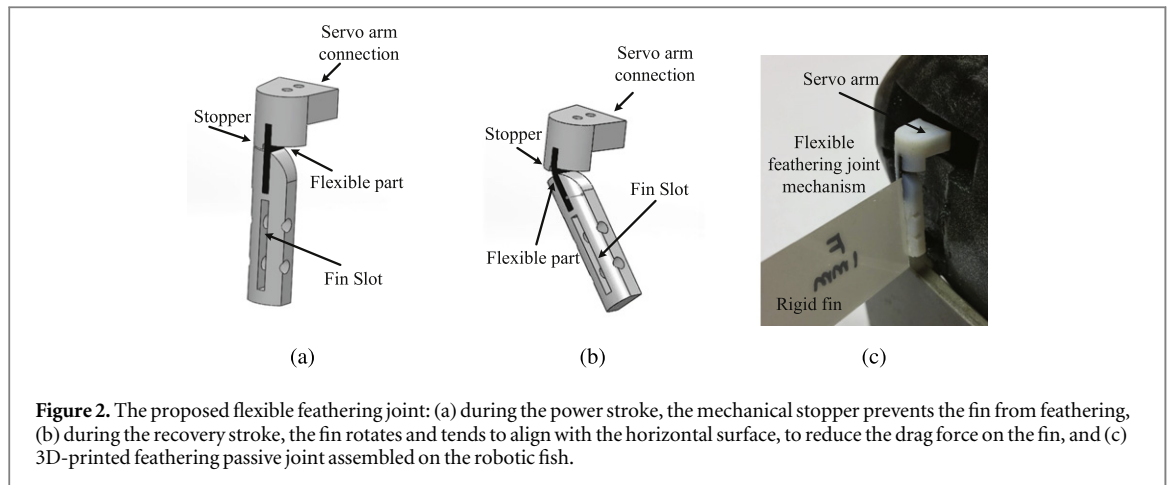


**Figure 2.** The proposed flexible feathering joint: (a) during the power stroke, the mechanical stopper prevents the fin from feathering, (b) during the recovery stroke, the fin rotates and tends to align with the horizontal surface, to reduce the drag force on the fin, and (c) 3D-printed feathering passive joint assembled on the robotic fish.

swimming is called drag-based labriform swim, and is illustrated in figure 1. In particular, the pectoral fin maintains the servo-prescribed rowing motion during the power stroke, to produce a maximum net thrust, while it rotates passively along the transverse axis (feathers) during the recovery stroke, to reduce the hydrodynamic drag on the fin.

The proposed feathering joint design is shown in figure 2. The entire joint mechanism consists of a rigid servo arm connector that connects the whole joint/fin structure to the servo motor, a mechanical stopper, a fin mount and a rectangular flexible piece (shown in black in figures 2(a) and 2(b)), serving as the feathering joint, which connects the fin mount structure to the servo arm connector. During the power stroke, the mechanical stopper enable the pectoral fin to maintain the rowing motion prescribed by the servo motor, as shown in figures 1(a) and 2(a), while during the recovery stroke, the flexible joint enables the fin to feather passively and reduce the hydrodynamic drag force, as shown in figures 1(b) and 2(b).

Flexible feathering joints are prototyped using a multi-material 3D printer (Connex 350 from Object), which is capable of simultaneously jetting rigid and flexible materials, resulting in seamless integration of the pliable and rigid components of the flexible joint mechanism, as shown in figure 2(c). All the rigid parts (servo arm connector and fin mount) are printed with the material RGD835 (VeroWhitePlus). Two different flexible materials, FLX980 (TangeBlackPlus), which is the most flexible material supported by the printer, and DM9850 (Digital Material 9850), which is stiffer than FLX980 but still flexible enough, are explored for the flexible part of the feathering joint structure. Other than different materials, it is also our goal to investigate the impact of joint dimensions on the propulsion performance. For this purpose, a total of four joints are printed, three using FLX980 and one using DM9850. All joints have width of 4 mm and thickness of 1 mm, to ensure adequate strength for surviving through extensive experiments. The three FLX980 joints have different values for their depth, 0.5 mm

1 mm and 1.5 mm, while the DM9850 joint has a depth of 0.5 mm. Here the joint depth refers to the extent of the gap between the top and bottom rigid elements on the side opposite to the mechanical stopper. The gap is negligible on the stopper side. The four joints, with their different combinations of materials and depths, enable a compact set of experiments for validating the proposed dynamic model and revealing design trade-offs. The joints are referenced as follows. Joint 'JF1', with FLX980 as the flexible material and depth of 0.5 mm, joint 'JF2' with FLX980 as the flexible material and depth of 1 mm, joint 'JF3' with FLX980 as the flexible material and depth of 1.5 mm, and finally, joint 'JF4' with DM9850 as the flexible material and depth of 0.5 mm.

### 3. Dynamic model of fin-actuated robotic fish incorporating the flexible feathering joint

#### 3.1. Hydrodynamic forces on the fin

In this section, first we describe the use of blade element theory in representing the hydrodynamic force on the fin, for a given fin movement pattern, which is determined by the (yet to solve) dynamics of the flexible joint, namely, the feathering dynamics. The hydrodynamic force is then incorporated into the dynamic model for the feathering motion, which is captured via a pair of torsional spring and damper. Finally, the total hydrodynamic forces and moments resulting from the fin mechanism are used to develop the dynamic model for the robotic fish propelled by the fins.

Adapted from [19], the blade element theory is used to evaluate the hydrodynamic forces on the pectoral fins. For all these calculations, we assume an anchored robotic fish body. This assumption is often adopted in the literature for similar problems [5, 39, 40]. While this simplification introduces modeling error, the resulting error is typically acceptable considering the much larger fin velocity comparing to the velocity of the robotic fish itself. For ease of

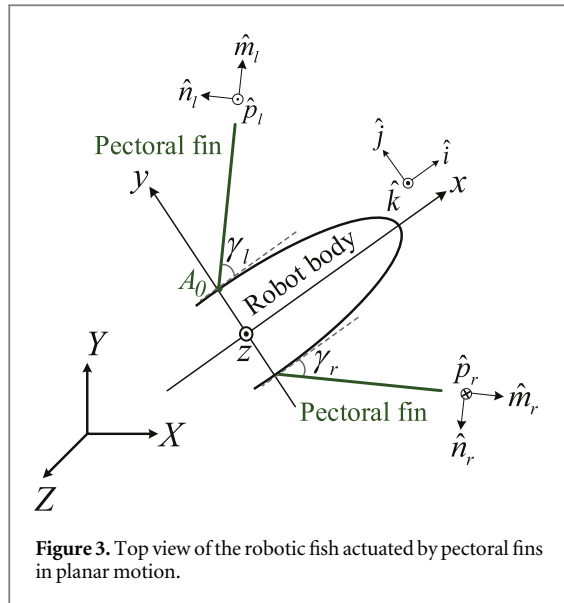


Figure 3. Top view of the robotic fish actuated by pectoral fins in planar motion.

calculation, the pectoral fin is considered to be rigid and rectangular with span length  $S$  and chord length (depth)  $C$ . Figure 3 shows the top view of a robotic fish, consisting of a rigid body and paired pectoral fins.  $[X, Y, Z]^T$  indicates the inertial coordinate system and  $[x, y, z]^T$  represents the body-fixed coordinate system, with corresponding unit vectors  $[\hat{i}, \hat{j}, \hat{k}]$ , which is attached to the center of mass of the robotic fish. We use  $[\hat{m}, \hat{n}, \hat{p}]$  to denote the unit vectors of the pectoral fin coordinate system, where subscripts  $r$  and  $l$  are used to represent right and left fins, respectively. Here  $\hat{m}$  is parallel and  $\hat{n}$  is perpendicular to the pectoral fin and  $\hat{p}$  is automatically formed by the right-hand orthonormal principle. The notation  $\vec{r}_{c_p} = c_p \hat{j}$  denotes the vector pointing from the robotic fish center of mass to the pectoral fin servo motor base (point  $A_0$ ).

We divide the pectoral fin movement cycle into power and recovery strokes, and study each separately. During the power stroke, the pectoral fin undergoes a rowing motion prescribed by the servo motor; therefore, the fin plane stays vertical and the hydrodynamic forces are restricted to the horizontal plane, as shown in figure 4. Here, all the calculations are done for the left pectoral fin, which can be extended to the right fin in a straightforward manner.

During the power stroke, the relation between the orthonormal unit vectors  $[\hat{m}, \hat{n}, \hat{p}]$  and the body-fixed coordinate system is given by

$$\hat{m} = \cos \gamma \hat{i} + \sin \gamma \hat{j}, \quad (1)$$

$$\hat{n} = -\sin \gamma \hat{i} + \cos \gamma \hat{j}, \quad (2)$$

$$\hat{p} = \hat{k}. \quad (3)$$

where  $\gamma$  is the prescribed angle of the servo arm with respect to the body heading  $\hat{i}$ .

In blade element theory, the hydrodynamic force  $dF_{h_p}(s, t)$  on each defined blade element,  $ds$ , at time  $t$ , is calculated as

$$dF_{h_p}(s, t) = -\frac{1}{2} C_n(\alpha(s, t)) \rho |\vec{v}_p(s, t)| C ds \hat{n}, \quad (4)$$

where  $\rho$  denotes the water density,  $\vec{v}_p(s, t)$  is the velocity of each blade element of the pectoral fin, and  $C_n$  is the normal force coefficient, which is dependent on the angle of attack of the blade,  $\alpha(s, t)$ . Here, we consider  $C_n = 3.4 \sin \alpha(s, t)$ , by utilizing an empirically evaluated model for insect wing which was used for a robotic fly [41] and robotic ‘boxfish’ [42]. Even though insects (or robotic insects) fly in air while robotic fish swim in water, the associated fluid dynamics will have similar behavior if their Reynolds numbers are close. In particular, the Reynolds number of the robotic fish in this work is at the order of  $10^3$ , which is close to the Reynolds number reported in [41] for the robotic fly (30–1000).

The velocity of each element,  $\vec{v}_p(s, t)$ , is expressed as

$$\begin{aligned} \vec{v}_p(s, t) &= v_{px} \hat{i} + v_{py} \hat{j} \\ &= \{-(l_1 + s) \dot{\gamma} \sin \gamma\} \hat{i} + \{(l_1 + s) \dot{\gamma} \cos \gamma\} \hat{j}, \end{aligned} \quad (5)$$

where  $l_1$  is the length of the servo arm.

The angle of attack of each blade element can be evaluated via

$$\tan \alpha = \frac{\langle v_p(s, t), \hat{n} \rangle}{\langle v_p(s, t), \hat{m} \rangle} = \frac{-v_{px} \sin \gamma + v_{py} \cos \gamma}{v_{px} \cos \gamma + v_{py} \sin \gamma}, \quad (6)$$

where  $\langle \cdot, \cdot \rangle$  denotes the inner product. With the anchored body assumption, it is easy to verify that the angle of attack is  $90^\circ$ .

The total hydrodynamic force acting on each pectoral fin is calculated by integrating the force density along the span length of the fin

$$\vec{F}_{h_p}(t) = \int_0^S dF_{h_p}(s, t). \quad (7)$$

On the other hand, during the recovery stroke, the pectoral fin undergoes a 3D motion. We modify the blade element theory, so that we have blades in both span and chord length of the fin, resulting in 2D elements, which we use to evaluate the hydrodynamic forces. The fin parameters during the recovery stroke are shown in figure 5, where  $\Lambda$  is the feathering angle that we need to find in order to fully know the pectoral fin dynamics. Note that the feathering angle  $\Lambda = 0$  during the power stroke.

The relationship between the pectoral fin coordinate system and the body-fixed coordinate system is as follows

$$\hat{m} = \cos \gamma \hat{i} + \sin \gamma \hat{j} + 0 \hat{k}, \quad (8)$$

$$\hat{n} = \sin \gamma \cos \Lambda \hat{i} - \cos \gamma \cos \Lambda \hat{j} - \sin \Lambda \hat{k}, \quad (9)$$

$$\hat{p} = -\sin \gamma \sin \Lambda \hat{i} + \cos \gamma \sin \Lambda \hat{j} - \cos \Lambda \hat{k}, \quad (10)$$

where  $\Lambda$  is the feathering angle defined with respect to  $-\hat{k}$ .

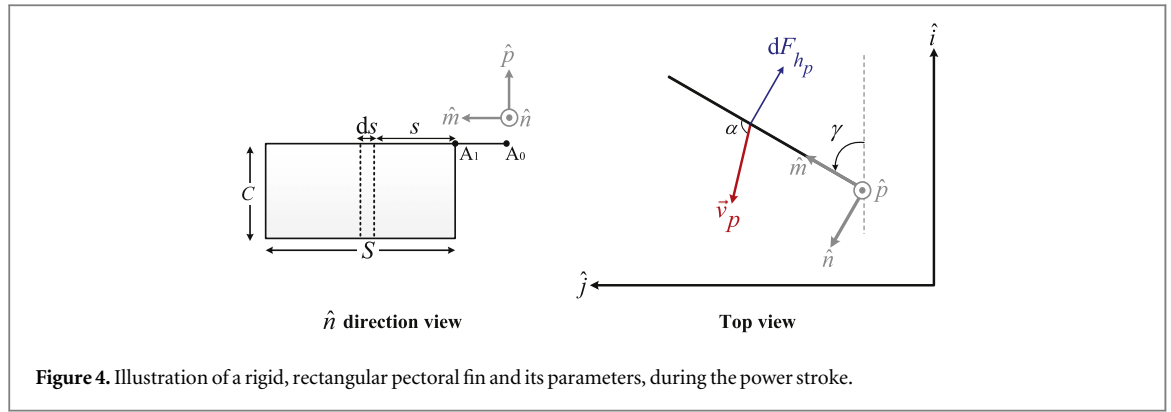


Figure 4. Illustration of a rigid, rectangular pectoral fin and its parameters, during the power stroke.

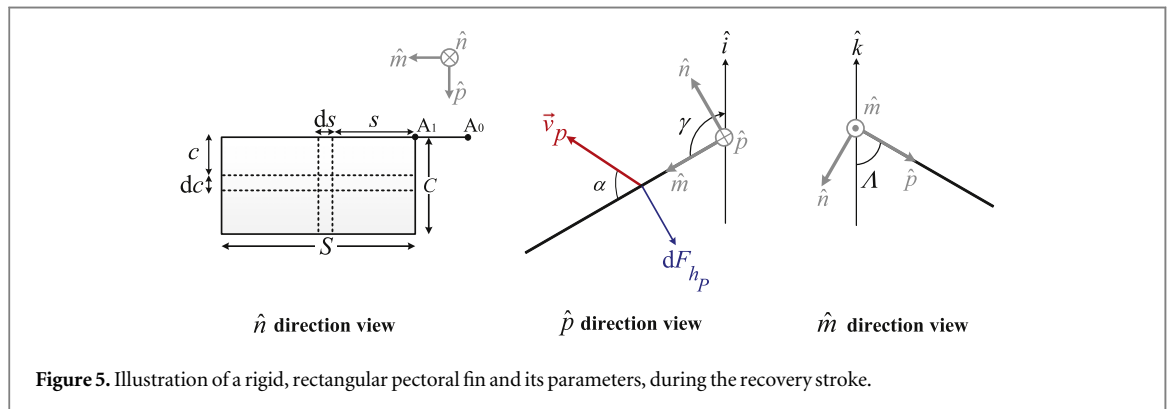


Figure 5. Illustration of a rigid, rectangular pectoral fin and its parameters, during the recovery stroke.

The blade element theory is revised to evaluate the hydrodynamic forces on a 2D element of the pectoral fin. The hydrodynamic drag force produced by each element  $dc ds$  during the recovery stroke is evaluated as

$$dF_{hp}(c, s, t) = -\frac{1}{2} C_n(\alpha(c, s, t)) \rho |\vec{v}_p(c, s, t)|^2 dc ds \hat{e}_{v_p} \quad (11)$$

where  $\hat{e}_{v_p}$  is a unit vector in the direction of  $\vec{v}_p(c, s, t)$ ,  $\alpha(c, s, t) = \text{atan}\left(\frac{v_p(c, s, t), \hat{n}}{v_p(c, s, t), \hat{m}}\right)$  is the angle of attack, and  $\vec{v}_p(c, s, t)$  is the velocity of each element  $dc ds$ , and is represented as

$$\begin{aligned} \vec{v}_p(c, s, t) &= v_{px} \hat{i} + v_{py} \hat{j} + v_{pz} \hat{k} \\ &= \{-(l_1 + s)\dot{\gamma} \sin \gamma - c\dot{\gamma} \cos \gamma \sin \Lambda - c\dot{\Lambda} \sin \gamma \cos \Lambda\} \hat{i} \\ &\quad + \{(l_1 + s)\dot{\gamma} \cos \gamma - c\dot{\gamma} \sin \gamma \sin \Lambda + c\dot{\Lambda} \cos \gamma \cos \Lambda\} \hat{j} \\ &\quad - \{c\dot{\Lambda} \sin \Lambda\} \hat{k}. \end{aligned} \quad (12)$$

We note that there is notation abuse associated with  $dF_{hp}$ ,  $\alpha$ , and  $\vec{v}_p$ , which depend only on  $s$  and  $t$  in (4) but depend on  $s$ ,  $c$ , and  $t$  in (11), and hope their meanings will be clear from the context. The total hydrodynamic force is evaluated by integrating the force density over the surface of the pectoral fin

$$\vec{F}_{hp}(t) = \int_0^S \int_0^C dF_{hp}(c, s, t). \quad (13)$$

### 3.2. Solving the feathering dynamics

During the power stroke, the rigid fin follows the servo motion ( $\Lambda = 0$ ), and the corresponding hydrodynamic force on the fin can be evaluated given the servo motion. On the other hand, during the recovery stroke, the evaluation of the hydrodynamic force (equation (11)) requires knowing the feathering angle  $\Lambda$ , which has to be solved for through the dynamics equation for the feathering joint.

The total force acting on the rigid fin is represented as

$$\vec{F}_2 = \vec{F}_{hp} - \vec{F}_{A_1} = m_p \frac{d\vec{v}_p(c, s, t)}{dt} \Big|_{s=\frac{S}{2}, c=\frac{C}{2}}, \quad (14)$$

where  $\vec{F}_{hp}$  is the hydrodynamic force on the rigid fin (calculated based on the equations presented in section 3.1),  $\vec{F}_{A_1}$  represents the force applied by the rigid fin (through the joint) on the servo arm, and  $m_p$  is the effective mass of the rigid pectoral fin, which contains the fin mass and the added mass (where the added mass is calculated base on a rigid plate moving in the water).

Since we need to find the feathering angle of the fin,  $\Lambda$ , the projection of the hydrodynamic force in  $\hat{n}$  direction produces the corresponding moment. The moment of the rigid fin relative to its pivot point is evaluated as

$$\vec{M}_{hp}(t) = \int_0^S \int_0^C \hat{c} \hat{p} \times dF_{hp}(c, s, t). \quad (15)$$

Here  $\vec{M}_{hp}$  is a function of  $\Lambda$  and  $\dot{\Lambda}$ . The moment produced by the flexible feathering joint, which is modeled as a pair of torsional spring and damper, is evaluated as

$$\vec{M}_{(S+D)} = (-K_S \Lambda - K_D \dot{\Lambda}) \hat{m}, \quad (16)$$

where  $K_S$  and  $K_D$  are the spring and damper coefficients used to model the flexible feathering joint.

The total moment equation of the rigid fin relative to its pivot point of feathering is written as

$$\vec{M}_2 = \vec{M}_{hp} + \vec{M}_{(S+D)} = -I_p \ddot{\Lambda}, \quad (17)$$

where  $I_p$  is the effective inertia of the rigid fin (which contains the fin inertia and the added inertia, and is calculated base on a rigid plate moving in the water) and  $\ddot{\Lambda}$  is the angular acceleration of the fin in  $\hat{m}$ -direction. By solving equation (17), the dynamics of the pectoral fin with a flexible feathering joint during the recovery stroke is fully described.

### 3.3. Hydrodynamic forces and moments on the robotic fish

The hydrodynamic force transmitted to the servo arm can be obtained as  $-\vec{F}_{A_1} = \vec{F}_{hp} - m_p \frac{d\vec{v}_p(c, s, t)}{dt} \Big|_{s=\frac{S}{2}, c=\frac{C}{2}}$ . The total force exerted by the arm on the robot body is

$$\vec{F}_h = F_{h_x} \hat{i} + F_{h_y} \hat{j} = \vec{F}_{A_1}. \quad (18)$$

The moment applied by the fin on the body is represented as

$$\vec{M}_h = M_{h_z} \hat{k} = c_p \hat{j} \times \vec{F}_{A_1}. \quad (19)$$

Other than hydrodynamic forces and moment transmitted from the pectoral fins, the robotic fish body experiences drag force  $F_D$ , lift force  $F_L$ , and drag moment  $M_D$ , which can be represented as [10, 28, 39]

$$F_D = \frac{1}{2} \rho V_C^2 S_A C_D, \quad (20)$$

$$F_L = \frac{1}{2} \rho V_C^2 S_A C_L \beta, \quad (21)$$

$$M_D = -C_M \omega_{C_z}^2 \text{sgn}(\omega_{C_z}), \quad (22)$$

where  $V_C$  is the linear velocity magnitude of the robotic fish body,  $\omega_{C_z}$  is the angular velocity of the body about the  $z$ -axis,  $\rho$  is the mass density of water,  $S_A$  is the wetted surface area for the body,  $\beta$  is the angle of attack of the body, formed by the direction of body velocity vector with respect to the  $x$ -axis.  $C_D$ ,  $C_L$  and  $C_M$  are the dimensionless drag force, lift force, and damping drag moment coefficients, respectively, and  $\text{sgn}(\cdot)$  is the signum function.

### 3.4. Rigid-body dynamics of a pectoral fin-actuated robotic fish undergoing planar motion

The dynamic equations of rigid body undergoing planar motion in the body-fixed coordinates are represented as [37, 43, 44]

$$(m_b - m_{a_x}) \dot{V}_{C_x} = (m_b - m_{a_y}) V_{C_y} \omega_{C_z} + f_x, \quad (23)$$

$$(m_b - m_{a_y}) \dot{V}_{C_y} = -(m_b - m_{a_x}) V_{C_x} \omega_{C_z} + f_y, \quad (24)$$

$$(I_z - I_{a_z}) \dot{\omega}_{C_z} = \tau_z, \quad (25)$$

where  $m_b$  is the robotic fish actual mass,  $-m_{a_x}$  and  $-m_{a_y}$  represent the added mass effects along the  $x$  and  $y$  directions of the body-fixed coordinates, respectively.  $I_z$  is the robot inertia and  $-I_{a_z}$  is the added inertia of the robot about the  $z$ -axis. The variables  $f_x$ ,  $f_y$  and  $\tau_z$  indicate the external hydrodynamic forces and moment exerted on the fish body center of mass, which are induced by the pectoral fin motion and the interaction of the robotic fish body with the surrounding fluid, which can be described as

$$f_x = F_{h_x} - F_D \cos \beta + F_L \sin \beta, \quad (26)$$

$$f_y = F_{h_y} - F_D \sin \beta - F_L \cos \beta, \quad (27)$$

$$\tau_z = M_{h_z} + M_D. \quad (28)$$

Finally, the kinematic equations for the robot in the inertial coordinate system are described as [39],

$$\dot{X} = V_{C_x} \cos \psi - V_{C_y} \sin \psi, \quad (29)$$

$$\dot{Y} = V_{C_y} \cos \psi + V_{C_x} \sin \psi, \quad (30)$$

$$\dot{\psi} = \omega_{C_z}, \quad (31)$$

where  $\psi$  denote the angle between the  $x$ -axis and  $X$ -axis.

## 4. Experimental results

### 4.1. Robotic fish prototype and experimental setup

Experiments are performed to study the performance of a robotic fish with flexible feathering joint and validate the proposed mathematical model. The robotic fish body is designed in SolidWorks software and 3D-printed, as shown in figure 6. The body is about 15 cm long, 8 cm high and 4.6 cm wide without the pectoral and caudal fins, and weighs close to 0.3 kg. An Arduino pro mini microcontroller board is incorporated in the robot to realize the control of servos. The robot body also houses a power converter printed-circuit board with voltage regulators for the motor and electronics. The motors used for actuation of the pectoral and caudal fins are Traxxas 2065 waterproof servos with maximum speed of 200°/s. Although the robot is capable of moving its caudal fin, tail actuation is not included in this study. The servomotors are programmed to rotate each pectoral fin according to

$$\gamma(t) = \gamma_A \sin(\omega_\gamma t) + 90^\circ, \quad (32)$$

where  $\gamma_A$  is the amplitude in degrees and  $\omega_\gamma$  denotes the angular frequency of fin flapping. The pectoral fins are made of a light plastic material (polypropylene) that has 0.5 mm thickness with Young's modulus of approximately 2 GPa, which is considered to be almost rigid.

As shown in figure 7, the experiments are conducted in a water tank that measures 2 feet wide, 6 feet

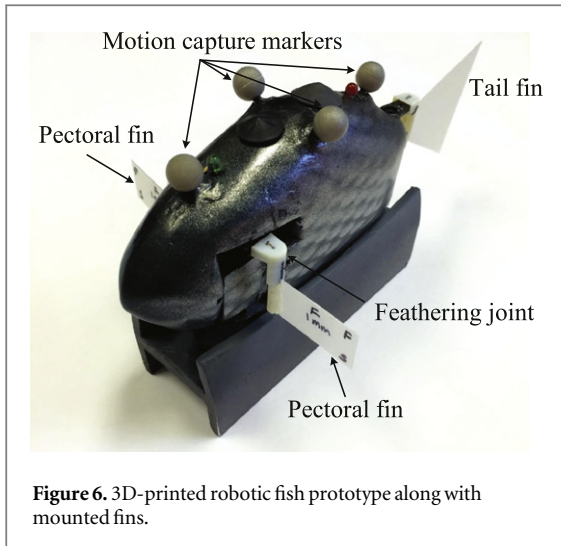


**Figure 6.** 3D-printed robotic fish prototype along with mounted fins.

long, and 2 feet deep. The tank is equipped with a motion capture system from NaturalPoint, which contains four Optitrack Flex 13 cameras along with Motive software to capture the motion of robotic fish. Two different experiments are conducted to evaluate the proposed dynamic model. First, the robotic fish is studied when the body is anchored to measure the feathering angle, and second, free-swimming of the robotic fish is run to measure the forward swimming velocity, turning radius, and turning period. All the measurements are done approximately 30 s after the robot initiated swimming to ensure that it has reached steady-state motion. The experiment for each setting is repeated 10 times. At the end, the captured videos are analyzed by the Motive software to extract the steady-state speed for the forward swimming, and the turning radius and period for the turning motion.

#### 4.2. Parameter identification

The parameters of the mathematical model are either measured directly or identified experimentally as follows: the body inertia about  $z$ -axis is evaluated as  $I_z = \frac{1}{5}m_b(a^2 + c^2)$ , where  $a = \frac{\text{Body length}}{2}$  and  $c = \frac{\text{Body width}}{2}$  are semi-axis lengths of the body [10]. The added masses, added inertia and wetted surface are calculated by approximating the robot body as a prolate spheroid accelerating in the fluid [10, 45]. The parameters used in simulations are listed in table 1.

The robotic fish drag and lift coefficients,  $C_D$ ,  $C_L$ , and  $C_M$ , are identified empirically using the collected data from the robotic fish equipped with rigid joints for the pectoral fins. With rigid joints, we need to have different power and recovery stroke speeds to produce a net thrust [33]. This ratio is indicated as  $\frac{P}{R} \left( \frac{\text{Power stroke speed}}{\text{Recovery stroke speed}} \right)$ , which is equal to 1 for the symmetric fin flapping. Here, we experiment with the cases of  $\frac{P}{R} = 2, 3, 4$ , and 5. The experimental results for both forward and turning swimming motions of the robotic fish with  $\frac{P}{R} = 2$  are used to identify the body parameters,

where turning is realized by actuating one pectoral fin only.  $C_D$ ,  $C_L$ , and  $C_M$  are tuned to match the forward velocity, turning radius, and turning period obtained in simulation with the experimental measurement when the power stroke is completed in 0.5 s and 0.3 s, respectively. The fin-beat amplitude is set to 25°. The identified coefficients are  $C_D = 0.42$ ,  $C_L = 4.86$ , and  $C_M = 7.6 \times 10^{-4} \text{ Kg m}^{-2}$ . These parameters are then used in independent model validation for all other cases using the flexible feathering joint.

Among all the feathering joints mentioned in section 2, joint 'JF1' results in the highest forward velocity in the tested frequency range. So, without the loss of generality, this joint is chosen to perform the model validation. To identify the spring and damper coefficients for this joint,  $K_S$  and  $K_D$  are tuned to match the forward swimming velocity of the robotic fish obtained in simulation with the experimental measurements for fin-beat frequencies of 1 Hz, 1.5 Hz and 2 Hz. The coefficients are identified as  $K_S = 1.31 \times 10^{-4} \text{ N m}$  and  $K_D = 4.64 \times 10^{-5} \text{ N m s}$ . These parameters are then used for model validation of various other cases involving the same feathering joint.

#### 4.3. Comparison between flexible feathering and rigid joints

First, we provide a comparison on the forward swimming velocity of the robotic fish with the flexible feathering joint, with that of a rigid joint. Here, rigid joint refers to a rigid connection between the servo arms and the pectoral fins. For the rigid joint case, in order to have a net thrust, we use different power and recovery stroke speeds, introduced in section 4.2. Figure 8(a) provides the experimental results on forward swimming velocity with the rigid joint, where  $\frac{P}{R} = 1, 2, 3, 4, 5$ , and with the flexible feathering joint 'JF1', over different power stroke times. Figure 8(b) presents the same results in terms of the effective fin-beat frequency. Here, the effective fin-beat frequency is calculated as  $\frac{1}{T}$ , where  $T$  is the period of each fin-beat cycle, combining both power and recovery strokes. The servos are programmed to run up to the limit of 200°/s, which refers to the rightmost point in each curve of figure 8(b). From figure 8, one can conclude that, the performance of the flexible feathering joint outperforms the rigid joint case at higher frequencies (1.3 Hz and above). For lower fin-beat frequencies, the rigid joint cases outperform the flexible feathering joint. Note that the relationship between the flapping frequency and the swimming speed is almost linear up to a threshold value for the flapping frequency, which is observed naturally in fish [46].

#### 4.4. Dynamic model validation

This subsection describes the experiments carried out on the robotic fish with flexible feathering joint, to validate the proposed mathematical model. Two kinds

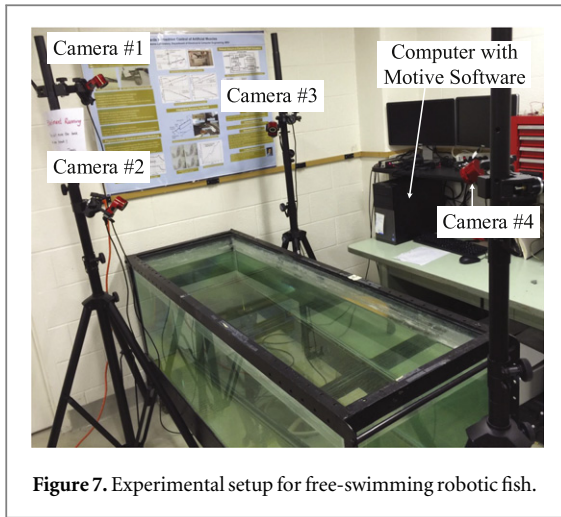


Figure 7. Experimental setup for free-swimming robotic fish.

of experiments are performed in still water for validation purposes. For the first set of experiments, the robot body is fixed using a bracket. The pectoral fins are actuated with  $\gamma(t) = 25^\circ \sin(\omega_\gamma t) + 90^\circ$ . The motion of the right pectoral fin is tracked from the side ( $xz$  plane), using a Casio Exilim (EX-FH25) high-speed camera, recording at 40 frames per second. The videos are then processed and the maximum feathering angle with respect to  $-\hat{k}$  is measured and compared to those predicted by the model. Figure 9 shows the maximum feathering angle during the recovery stroke, in both simulation and experiments at different fin-beat frequencies. The model is able to capture the maximum feathering angle well for all frequencies up to 1.5 Hz. For higher frequencies, the discrepancy between the model prediction and the measurement starts to grow. This can be attributed to the constraint of the fabrication, which imposes a limitation on the feathering angle of the joint.

For the second set of experiments, the robotic fish is allowed to swim freely in the tank. Both forward swimming and turning are enabled with the pectoral fins incorporating the flexible feathering joints. Figure 10 shows the experimental and simulation results where the forward swimming velocities of the robotic fish are plotted at different fin-beat frequencies. The forward swimming velocities of the robotic fish is reported both in  $\text{cm s}^{-1}$  and  $\text{BL s}^{-1}$  scales. Figures 11 and 12 show similar comparisons on the turning radius and turning period of a free-swimming robotic fish. The results of figures 10–12 show that the proposed model is able to capture the motion of the robotic fish with flexible feathering joints very well. In particular, for the tested frequency range, the forward swimming velocity increases with the fin-beat frequency. In the turning case, the turning period (the time it takes to complete one turn) drops with the increasing fin-beat frequency, which matches with one's intuition, and the turning radius increases with fin-beat frequency.

Table 1. Identified model parameters.

Component	Parameter	Value	Unit
Body	Mass ( $m_b$ )	0.295	Kg
	Inertia ( $I_z$ )	$4.26 \times 10^{-4}$	$\text{Kg m}^{-2}$
	$-m_{a_x}$	0.095	Kg
	$-m_{a_y}$	0.1794	Kg
	$-I_{a_z}$	$2.7 \times 10^{-5}$	$\text{Kg m}^{-2}$
	Wet surface area ( $S_A$ )	0.0325	$\text{m}^2$
	Drag coef. ( $C_D$ )	0.42	—
	Lift coef. ( $C_L$ )	4.86	—
	Moment coef. ( $C_M$ )	$7.6 \times 10^{-4}$	$\text{Kg m}^{-2}$
	Fin	Length ( $S$ )	0.035
Depth ( $C$ )		0.02	m
Servo arm length ( $l_i$ )		0.01	m
Effective mass ( $m_p$ )		0.0166	Kg
Effective inertia ( $I_p$ )		$3.32 \times 10^{-6}$	$\text{Kg m}^{-2}$
Distance from body center			
to servo base, $c_p$		0.025	m
Water density ( $\rho$ )	1000	$\text{Kg m}^3$	

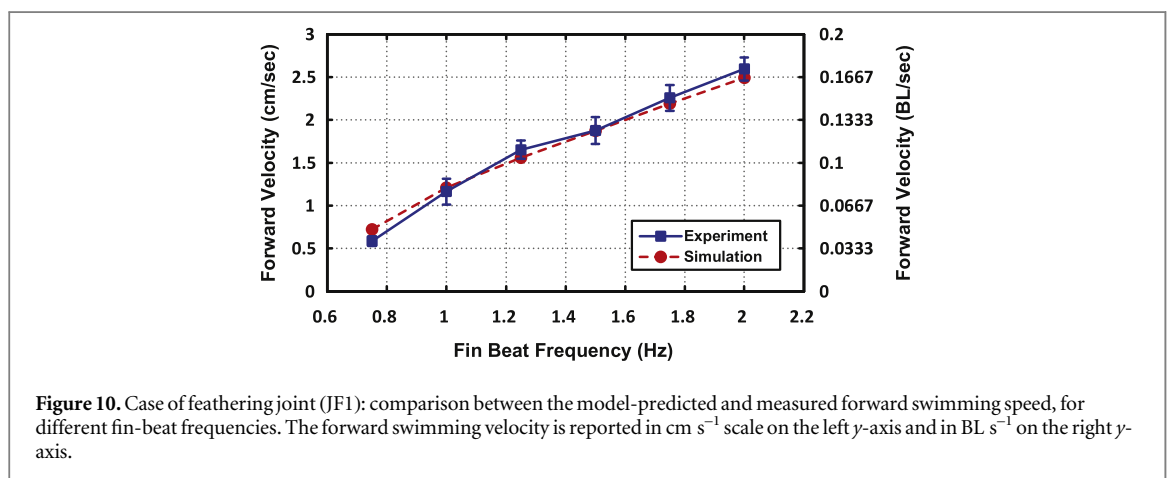
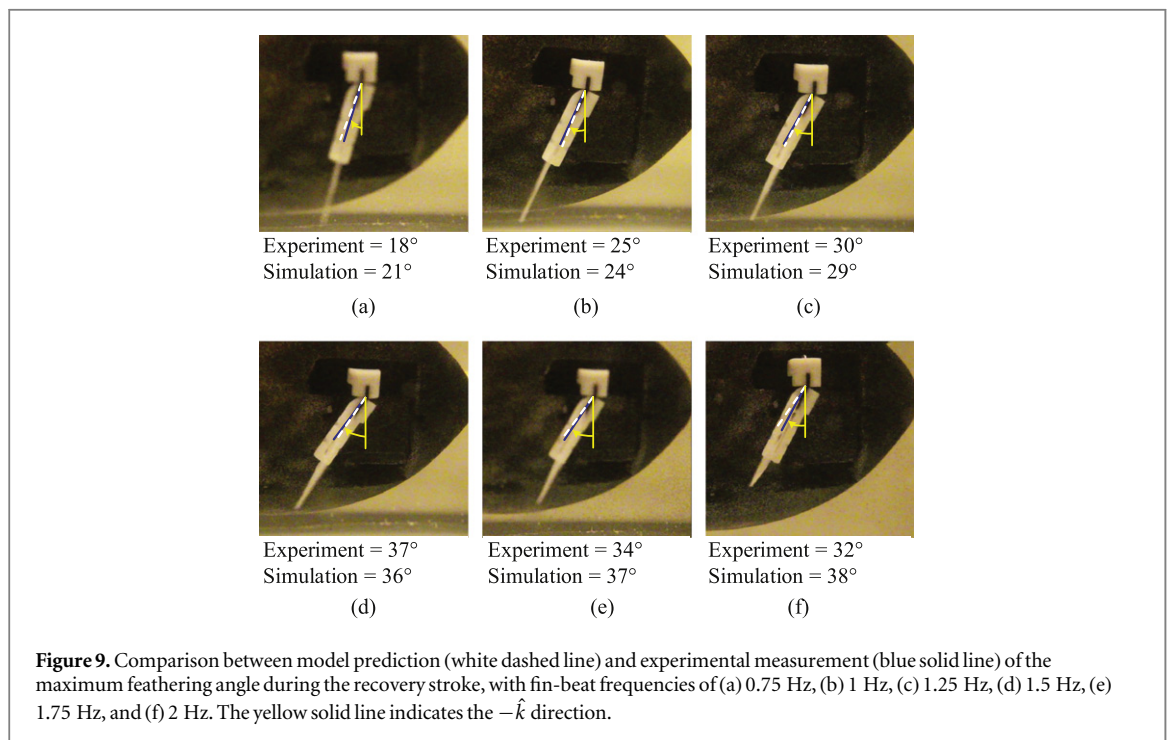
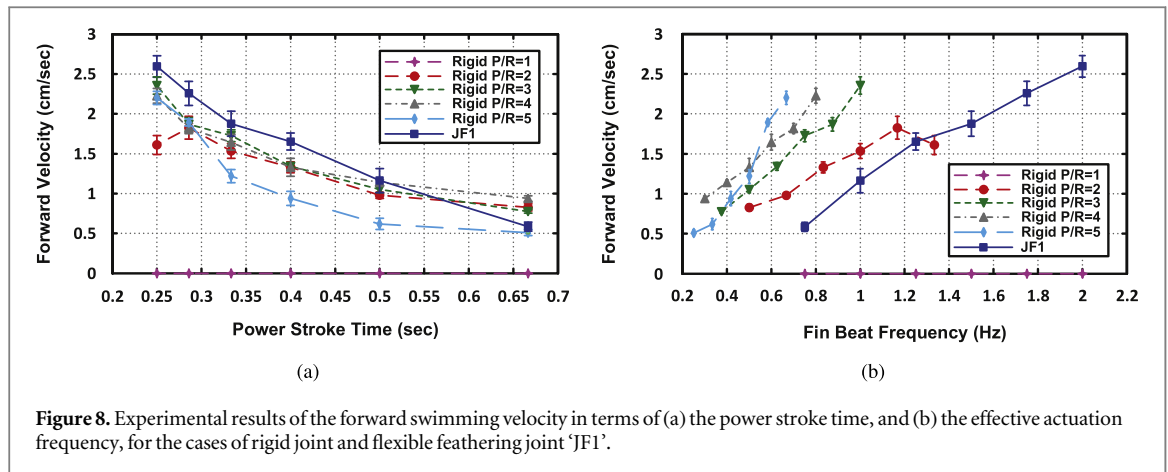
## 5. Effect of flexible joint depth and stiffness

Here, we study the effect of different parameters of the flexible feathering joint on its performance. As described in [47], the stiffness of the torsional spring constant is evaluated as

$$K_S = \frac{Edh^3}{12l}, \quad (33)$$

where  $h$  is the thickness,  $l$  is the length (which corresponds to the depth in the case of the proposed flexible joint),  $d$  is the width, and  $E$  is the Young's modulus of the flexible material used for the passive joint. The damper coefficient  $K_D$  is evaluated as  $K_D = \kappa K_S$ , where  $\kappa$  is a proportional constant. Keeping the width and thickness of the joint constant, the spring coefficient can be varied by changing the depth ( $l$ ) and stiffness ( $E$ ) of the flexible joint. This study will let us further validate the proposed mathematical model and provides useful information on the joint optimization.

We choose three different depth for the flexible feathering joint made of FLX980 material, 0.5 mm, 1 mm and 1.5 mm (Joints JF1, JF2, and JF3). The spring and damper constants for JF2 and JF3 are calculated using equation (33), where the Young's modulus ( $E$ ) and  $\kappa$  values are kept the same as the ones for JF1. Figure 13 shows the model prediction and experimental results of forward swimming velocity at different fin-beat frequencies, for different flexible feathering joint lengths. The joint JF1 (least flexible among the three) has the best performance among the three joints in the higher fin-beat frequencies (higher than 1.75 Hz). For lower frequencies, joint JF3 (most flexible among the three) outperforms the other two. So we can conclude that the more flexible joint performs better at lower frequencies, while the stiffer joint has a better performance at higher frequencies. We



can see that the model is able to capture the joint depth-dependence of the forward swimming velocity effectively for all three cases. Here, the experimental

limit for the actuation frequency is 2 Hz, so we have extended the simulation results to fin-beat frequency of 3 Hz in order to capture the performance trend of

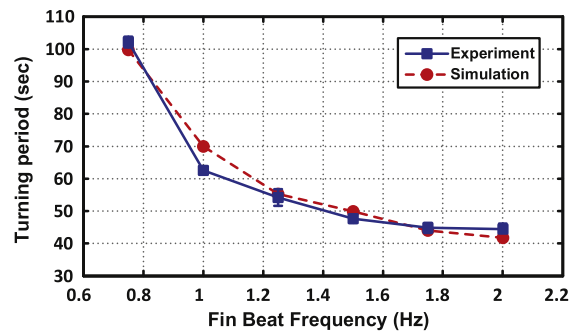


**Figure 11.** Case of feathering joint (JF1): comparison between the model-predicted and measured turning period, for different fin-beat frequencies.

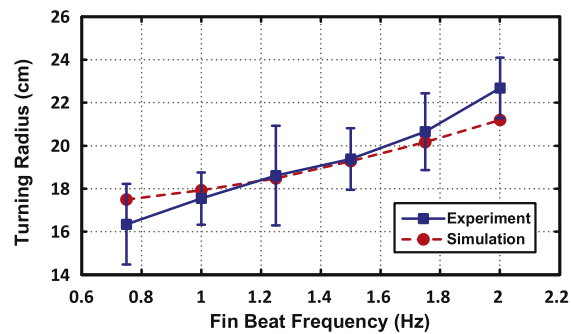


**Figure 12.** Case of feathering joint (JF1): comparison between the model-predicted and measured turning radius, for different fin-beat frequencies.

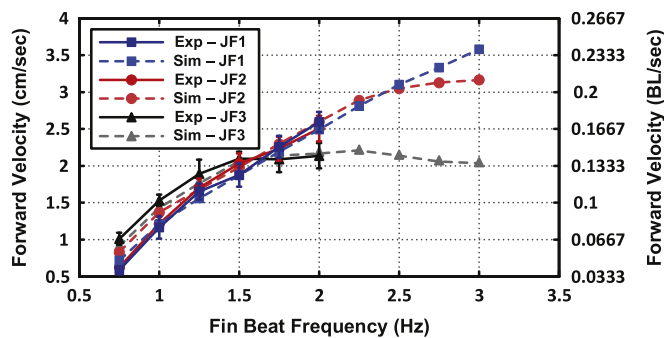


**Figure 13.** Model prediction and experimental measurement of the forward swimming velocity of the robotic fish using three different flexible feathering joints, made of FLX980, with different depths. The forward swimming velocity is reported in  $\text{cm s}^{-1}$  scale on the left  $y$ -axis and in  $\text{BL s}^{-1}$  on the right  $y$ -axis.

each joint. The forward swimming speed will drop after reaching an optimal frequency for each case.

Finally, we investigate the effect of changing the stiffness ( $E$ ) of the joint on the robotic fish performance. Here, we choose two flexible feathering joints with the same dimension, one using FLX980 as the flexible material, joint JF1, and the other using DM9850 as the flexible material, joint JF4. The spring and damper coefficients for JF4 are identified to be  $K_S = 0.0018 \text{ N m}$  and  $K_D = 0.0064 \text{ N m s}$  using the same method described in section 4.2, and are kept the same for model prediction of all other cases using the same joint. The comparison of forward swimming velocity using these two joints are

reported in figure 14. It can be seen that there is good match between the model prediction and experimental data. Overall, the joint JF1 outperforms JF4 at lower frequencies, while the joint JF4 starts to outperform joint JF1 at higher frequencies. Again, we have extended the model prediction results to capture the performance of the joints at higher frequencies.

## 6. Mechanical efficiency

In this section, we calculate the propulsive efficiency of the robotic fish swimming with the flexible feathering joint for the pectoral fins. The efficiency during the

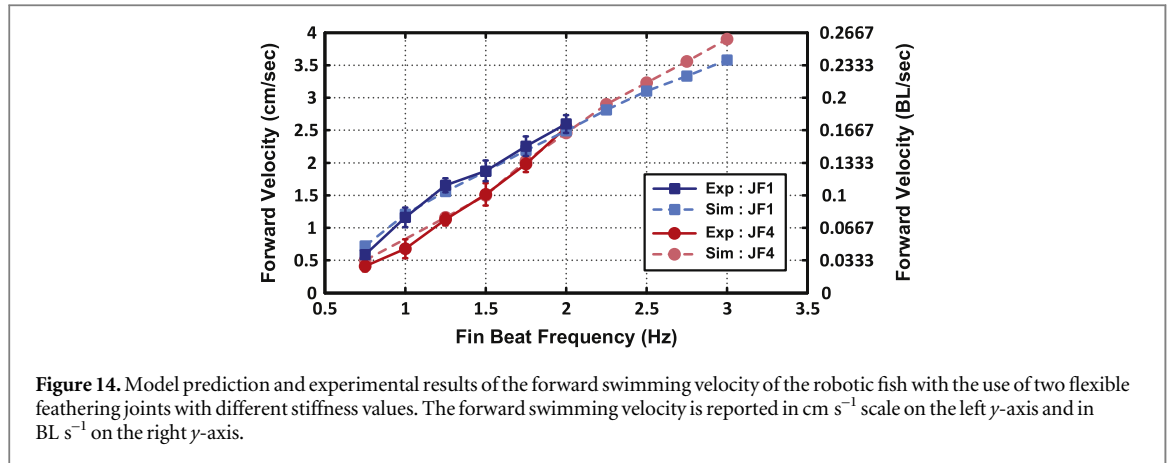


**Figure 14.** Model prediction and experimental results of the forward swimming velocity of the robotic fish with the use of two flexible feathering joints with different stiffness values. The forward swimming velocity is reported in  $\text{cm s}^{-1}$  scale on the left  $y$ -axis and in  $\text{BL s}^{-1}$  on the right  $y$ -axis.

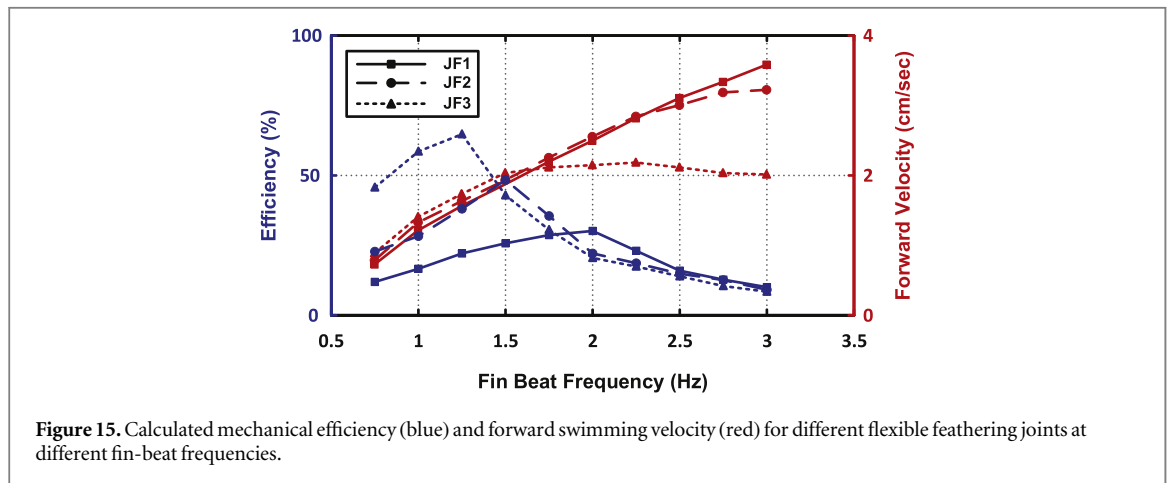


**Figure 15.** Calculated mechanical efficiency (blue) and forward swimming velocity (red) for different flexible feathering joints at different fin-beat frequencies.

steady-state swimming is calculated as [19]

$$\eta = \frac{W_b}{W_T}, \quad (34)$$

where  $W_b$  is the amount of useful work needed to propel the robotic fish and  $W_T$  is the total work done by the pectoral fins for each fin-beat cycle. This efficiency is called mechanical efficiency, since the energy losses, such as frictional losses or the power used to run the motors, are not considered in the calculations. During steady-state swimming, when the robot swims with a constant speed  $V_{C_{\text{mean}}}$ , the drag force acting on the body is balanced by the thrust force  $F_T$ . So we have

$$F_T = \frac{1}{2} \rho V_{C_{\text{mean}}}^2 S_A C_D. \quad (35)$$

So the useful propulsive power is calculated by multiplying thrust force,  $F_T$ , by the constant speed,  $V_{C_{\text{mean}}}$ , resulting in the useful work

$$W_b = F_T V_{C_{\text{mean}}} T_0 = \frac{1}{2} \rho V_{C_{\text{mean}}}^3 S_A C_D T_0, \quad (36)$$

where  $T_0 = T_p + T_R$  denotes the total duration of each fin-beat cycle, consists of duration of power and recovery strokes, where  $T_p = T_R = \frac{T_0}{2}$ . Note that even at the steady-state, the actual velocity is not a constant;

instead, it periodically fluctuates around some value. Therefore,  $V_{C_{\text{mean}}}$  in equation (35) is evaluated by the distance traveled over  $N$  cycles (for example,  $N = 10$ ) divided by  $NT_0$ .

The total work done by the paired pectoral fins,  $W_T$ , is obtained as

$$W_T = 2 \int_{t_0}^{t_0+T_p} \max \left\{ 0, \int_0^S dF_{h_p}(s, t) \cdot \vec{v}_p(s, t) \right\} dt + 2 \int_{t_0+T_p}^{t_0+T_p+T_R} \max \left\{ 0, \int_0^S \int_0^C dF_{h_p}(c, s, t) \cdot \vec{v}_p(c, s, t) \right\} dt, \quad (37)$$

where,  $t_0$  denotes the beginning of a fin-beat cycle and  $\cdot$  denotes the inner product. Note that at some time instants  $t$ , the instantaneous mechanical power exerted by pectoral fins on water could be negative; however, since the servos cannot reclaim this energy from water, we treat the instantaneous power at such  $t$  as zero, which explains the operator  $\max \{0, \cdot\}$  in equation (37).

Figure 15 shows the results for calculated mechanical efficiency, along with the corresponding forward swimming velocity, for joints JF1, JF2 and JF3. Joint JF3 has

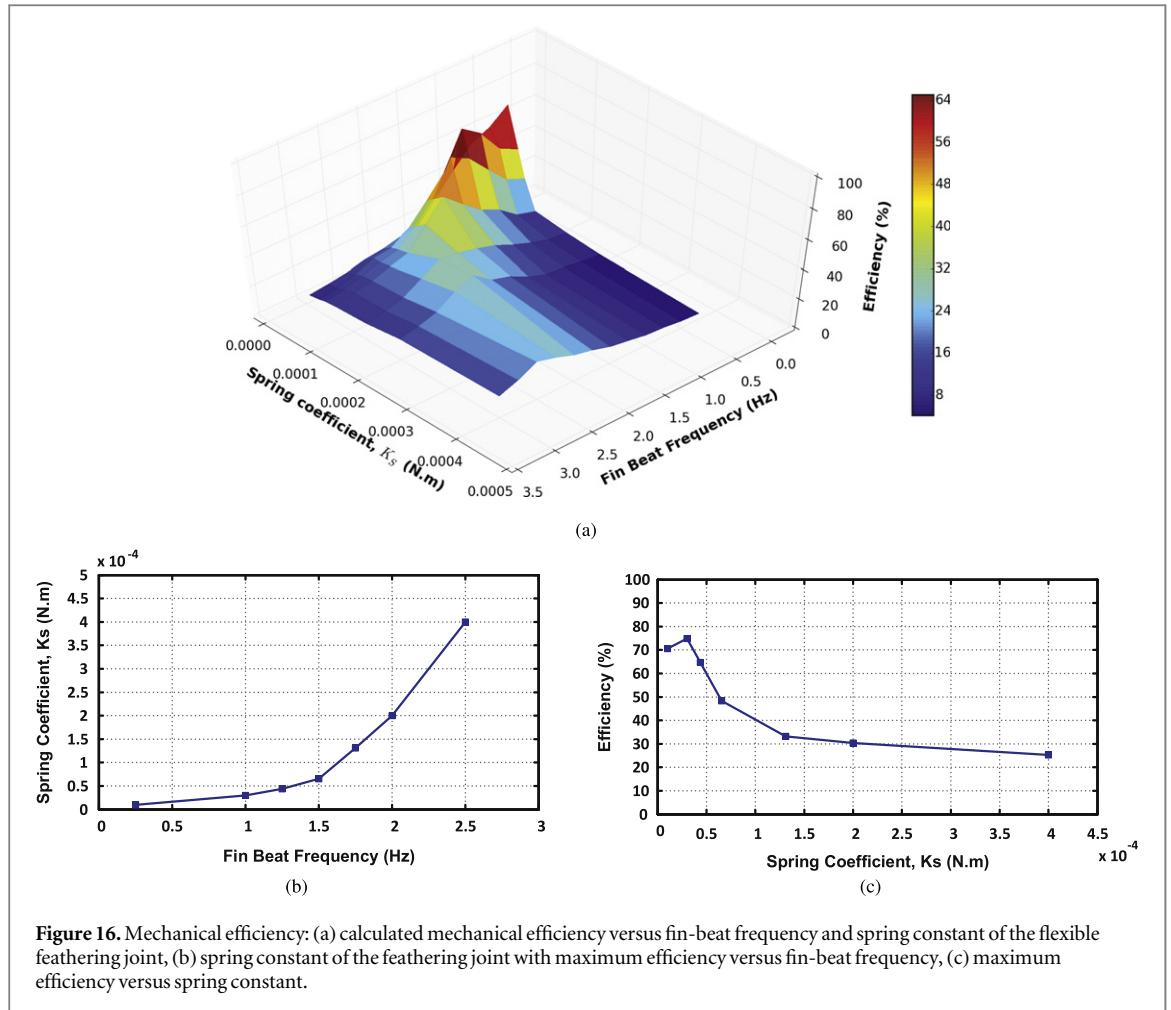


**Figure 16.** Mechanical efficiency: (a) calculated mechanical efficiency versus fin-beat frequency and spring constant of the flexible feathering joint, (b) spring constant of the feathering joint with maximum efficiency versus fin-beat frequency, (c) maximum efficiency versus spring constant.

highest efficiency at lower frequencies and joint JF1 is the most efficient at higher frequencies. Each joint has a maximum efficiency at a certain frequency. So we can conclude that a more flexible joint (JF3) is more efficient at lower frequencies and a less flexible joint (JF1) is more efficient at higher frequencies. Figure 16(a) shows the efficiency curve versus different fin-beat frequencies and spring constant values ( $K_s$ ). This figure shows that the robotic fish performs more efficiently in lower fin-beat frequencies with more flexible feathering joints up to a certain optimal stiffness. Figure 16(b) shows the spring constant of the feathering joints that have maximum mechanical efficiency in different fin-beat frequencies. From this figure, we can conclude that, the more flexible feathering joints are performing more efficiently at lower fin-beat frequencies, while the stiffer joints act more efficiently at higher frequencies. Note that, there is an optimal point for the maximum efficiency among all the feathering joints. From figure 16(c), one can see there is an optimal spring constant for the maximum efficiency. For any joint stiffer or more flexible than this optimal amount, the efficiency starts to drop. Note that a similar trend is observed in [48–51]. Overall, figures 15 and 16 indicate that the optimization of the flexible joint presents an interesting, multi-objective design problem that involves consideration of the joint stiffness, dimension, and the frequency of fin operation. The proposed

dynamic model in this paper shows promise in addressing the optimal design problem.

Table 2 presents the mechanical efficiency and Strouhal number for joints JF1, JF2, and JF3. Here the Strouhal number of the robotic fish is calculated as

$$St = \frac{fA}{V_{C_{mean}}}, \quad (38)$$

where  $f$  is the flapping frequency,  $A$  is the flapping amplitude for pectoral fin, and  $V_{C_{mean}}$  is the average swimming speed. Here the flapping amplitude  $A = 2S \sin \gamma$ , where  $S$  is the pectoral fin span length and  $\gamma$  is the angular amplitude of flapping [21, 30]. We observe consistent (negative) correlation between the efficiency and the Strouhal number. In particular, for each joint, at the fin-beat frequency where the efficiency achieves the maximum, the corresponding Strouhal number is the lowest. Note that the Strouhal number for biological fish is usually in the range of 0.05–0.6, and the numbers presented here are bigger than that range. The reason is that the robotic fish used in this study swims forward with its pectoral fins alone, which results in relatively slow speeds and thus relatively high Strouhal numbers comparing to its biological counterparts. From table 2, the robotic fish tends to have higher mechanical efficiency when its Strouhal number gets closer to the range for biological data.

**Table 2.** Mechanical efficiency versus the Strouhal number. For each joint, the highest mechanical efficiency (lowest Strouhal number) is boldfaced.

Frequency (Hz)	Joint JF1		Joint JF2		Joint JF3	
	Efficiency (%)	Strouhal number	Efficiency (%)	Strouhal number	Efficiency (%)	Strouhal number
0.75	11	3.7911	23	3.5436	46	2.3843
1	17	2.5447	28	2.4366	59	2.1383
1.25	22	2.3680	38	2.2194	<b>64</b>	<b>2.0430</b>
1.5	27	2.3653	<b>48</b>	<b>2.1865</b>	43	2.2005
1.75	29	2.2947	36	2.3189	30	2.5797
2	<b>32</b>	<b>2.2798</b>	22	2.3611	20	2.8766
2.25	23	2.3688	19	2.3437	17	3.0533
2.5	15	2.3857	15	2.4653	15	3.5051
2.75	13	2.4653	12	2.5583	10	4.0076
3	10	2.4790	9	2.7562	8	4.4154

## 7. Conclusion and future work

In this study, we have proposed a novel design for a flexible passive joint, which enables the pectoral fins to move similar to the drag-based labriform swimming mode. A dynamic model is presented for a robotic fish propelled by a pair of rigid pectoral fins connected to the actuators via the proposed flexible feathering joints. The joint enables the pectoral fin to be actuated symmetrically to row for power and recovery strokes, while providing feathering about the transverse axis during the recovery stroke to minimize the drag force. The combined rowing and feathering results in 3D movement of the pectoral fin, which needs to be captured properly in the modeling.

The blade element theory is used to evaluate the hydrodynamic forces on the pectoral fin during both power and recovery strokes. The flexible feathering joint is modeled as a pair of torsional spring and damper. A complete dynamic model for a robotic fish incorporating the proposed joints is also presented. To validate the proposed dynamic model, we have measured the feathering angle of an anchored robotic fish, along with the forward velocity, turning radius and period of the robot during free swimming, and compared those to the model predictions. Multiple flexible feathering joints have been explored to study the effect of depth and stiffness of the flexible part. The mechanical efficiency of the robotic fish in forward swimming is explored numerically, to understand the trade-offs in the joint design and operation frequency.

There are several directions in which the current work can be extended. First, in this paper, the main concern was to study the performance of flexible feathering joint, so all the studies are done on a rigid, rectangular pectoral fin. It is of interest to extend the current work to flexible pectoral fins of different shapes. Another interesting research direction will be to explore the interaction between the flexible caudal fin and the pectoral fins, in which case the caudal fin can be considered as a propulsion source to enable a

higher swimming speed, while the pectoral fins are used for accurate steering and turning.

## Acknowledgments

This work was supported in part by National Science Foundation (DBI-0939454, CNS-1059373, IIP 1343413, and IIS-1319602). The authors would like to thank John Thon for his contribution in assembling the robotic fish prototype.

## References

- [1] Triantafyllou M S and Triantafyllou G S 1995 An efficient swimming machine *Sci. Am.* **272** 64–71
- [2] Anderson J M and Chhabra N K 2002 Maneuvering and stability performance of a robotic tuna *Integr. Comp. Biol.* **42** 118–26
- [3] Bandyopadhyay P R 2002 Maneuvering hydrodynamics of fish and small underwater vehicles *Integr. Comp. Biol.* **42** 102–17
- [4] Yu J, Tan M, Wang S and Chen E 2004 Development of a biomimetic robotic fish and its control algorithm *IEEE Trans. Syst. Man Cybern. B* **34** 1798–810
- [5] Alvarado P V and Youcef-Toumi K 2006 Design of machines with compliant bodies for biomimetic locomotion in liquid environments *J. Dyn. Syst. Meas. Control* **128** 3–13
- [6] Lauder G V, Madden P G A, Mittal R, Dong H and Bozkurttas M 2006 Locomotion with flexible propulsors: I. Experimental analysis of pectoral fin swimming in sunfish *Bioinspir. Biomim.* **1** S25–34
- [7] Mittal R, Dong H, Bozkurttas M, Lauder G and Madden P 2006 Locomotion with flexible propulsors: II. Computational modeling of pectoral fin swimming in sunfish *Bioinspir. Biomim.* **1** S35
- [8] Liu J-D and Hu H 2006 Biologically inspired behaviour design for autonomous robotic fish *Int. J. Autom. Comput.* **3** 336–47
- [9] Ichikluzaki T and Yamamoto I 2007 Development of robotic fish with various swimming functions *Symp. on Underwater Technology and Workshop on Scientific Use of Submarine Cables and Related Technologies (Tokyo, Japan)* pp 378–83
- [10] Aureli M, Kopman V and Porfiri M 2010 Free-locomotion of underwater vehicles actuated by ionic polymer metal composites *IEEE/ASME Trans. Mechatronics* **15** 603–14
- [11] Nguyen Q S, Heo S, Park H C and Byun D 2010 Performance evaluation of an improved fish robot actuated by piezoceramic actuators *Smart Mater. Struct.* **19** 035030

- [12] Rossi C, Colorado J, Coral W and Barrientos A 2011 Bending continuous structures with smas: a novel robotic fish design *Bioinspir. Biomim.* **6** 045005
- [13] Wen L, Wang T M, Wu G H and Liang J H 2012 Hydrodynamic investigation of a self-propelled robotic fish based on a force-feedback control method *Bioinspir. Biomim.* **7** 036012
- [14] Kim S H, Shin K, Hashi S and Ishiyama K 2012 Magnetic fish-robot based on multi-motion control of a flexible magnetic actuator *Bioinspir. Biomim.* **7** 036007
- [15] Daou H E, Salumäe T, Chambers L D, Megill W M and Kruusmaa M 2014 Modelling of a biologically inspired robotic fish driven by compliant parts *Bioinspir. Biomim.* **9** 016010
- [16] Kancharala A K and Philen M K 2014 Study of flexible fin and compliant joint stiffness on propulsive performance: theory and experiments *Bioinspir. Biomim.* **9** 036011
- [17] Webb P W 1975 *Hydrodynamics and Energetics of Fish Propulsion* (Bulletin of the Fisheries Research Board of Canada 190) (Department of the Environment Fisheries and Marine Service) pp 1–156
- [18] Childress S 1981 *Mechanics of Swimming and Flying* (Cambridge Studies in Mathematical Biology No 2) 1st edn (Cambridge: Cambridge University Press)
- [19] Blake R 1983 *Fish Locomotion* (New York: Cambridge University Press)
- [20] Kato N 2000 Control performance in the horizontal plane of a fish robot with mechanical pectoral fins *IEEE J. Ocean. Eng.* **25** 121–9
- [21] Kodati P, Hinkle J, Winn A and Deng X 2008 Microautonomous robotic ostraciiform (MARCO): hydrodynamics, design and fabrication *IEEE Trans. Robot.* **24** 105–17
- [22] Low K H and Chong C W 2010 Parametric study of the swimming performance of a fish robot propelled by a flexible caudal fin *Bioinspir. Biomim.* **5** 046002
- [23] Chen Z, Shatara S and Tan X 2010 Modeling of biomimetic robotic fish propelled by an ionic polymer-metal composite caudal fin *IEEE/ASME Trans. Mechatronics* **15** 448–59
- [24] Ko Y, Na S, Lee Y, Cha K, Ko S Y, Park J and Park S 2012 A jellyfish-like swimming mini-robot actuated by an electromagnetic actuation system *Smart Mater. Struct.* **21** 057001
- [25] Bazaz Behbahani S and Tan X 2015 Dynamic modeling of robotic fish caudal fin with electrorheological fluid-enabled tunable stiffness *ASME Dynamic Systems and Control Conf. (DSCC) (Columbus, OH, USA 28–30 October 2015)* **DSCC2015-9879**
- [26] Sfakiotakis M, Lane D and Davies J 1999 Review of fish swimming modes for aquatic locomotion *IEEE J. Ocean. Eng.* **24** 237–52
- [27] Rosenberger L J 2001 Pectoral fin locomotion in batoid fishes: undulation versus oscillation *J. Exp. Biol.* **204** 379–94
- [28] Morgansen K A, Triplett B I and Klein D J 2007 Geometric methods for modeling and control of free-swimming fin-actuated underwater vehicles *IEEE Trans. Robot.* **23** 1184–99
- [29] Kato N and Furushima M 1996 Pectoral fin model for maneuver of underwater vehicles *Symp. on Autonomous Underwater Vehicle Technology (AUV) (Monterey, CA, USA)* pp 49–56
- [30] Sitorus P E, Nazaruddin Y Y, Leksono E and Budiyo A 2009 Design and implementation of paired pectoral fins locomotion of labriform fish applied to a fish robot *J. Bionic Eng.* **6** 37–45
- [31] Palmisano J, Ramamurti R, Lu K-J, Cohen J, Sandberg W and Ratna B 2007 Design of a biomimetic controlled-curvature robotic pectoral fin *IEEE Int. Conf. on Robotics and Automation (ICRA) (Rome, Italy)* pp 966–73
- [32] Kato N, Ando Y, Tomokazu A, Suzuki H, Suzumori K, Kanda T and Endo S 2008 Elastic pectoral fin actuators for biomimetic underwater vehicles *Bio-Mechanisms of Swimming and Flying* ed N Kato and S Kamimura (Japan: Springer) pp 271–82
- [33] Bazaz Behbahani S, Wang J and Tan X 2013 A dynamic model for robotic fish with flexible pectoral fins *IEEE/ASME Int. Conf. on Advanced Intelligent Mechatronics (AIM) (Wollongong, Australia)* pp 1552–7
- [34] Bazaz Behbahani S and Tan X 2014 A flexible passive joint for robotic fish pectoral fins: design, dynamic modeling, and experimental results *IEEE/RSJ Int. Conf. on Intelligent Robots and Systems (IROS) (Chicago, IL, USA)* pp 2832–8
- [35] Gibb A, Jayne B and Lauder G 1994 Kinematics of pectoral fin locomotion in the bluegill sunfish *lepomis macrochirus* *J. Exp. Biol.* **189** 133–61
- [36] Westneat M W and Walker J A 1997 Applied aspects of mechanical design, behavior, and performance of pectoral fin swimming in fishes *Proc. of Unmanned, Untethered, Submersible Technology (UUST)* pp 83–91
- [37] Bazaz Behbahani S and Tan X 2014 Design and dynamic modeling of a flexible feathering joint for robotic fish pectoral fins *ASME Dynamic Systems and Control Conf. (DSCC) (San Antonio TX, USA, 22–24 October 2014)* p V001T05A005
- [38] Bazaz Behbahani S and Tan X 2016 Design and modeling of flexible passive rowing joints for robotic fish pectoral fins *IEEE Trans. Robot.*, conditionally accepted
- [39] Wang J, McKinley P K and Tan X 2015 Dynamic modeling of robotic fish with a base-actuated flexible tail *J. Dyn. Syst. Meas. Control* **137** 011004
- [40] Kopman V and Porfiri M 2013 Design, modeling, and characterization of a miniature robotic fish for research and education in biomimetics and bioinspiration *IEEE/ASME Trans. Mechatronics* **18** 471–83
- [41] Deng X, Schenato L, Wu W C and Sastry S 2006 Flapping flight for biomimetic robotic insects: I. System modeling *IEEE Trans. Robot.* **22** 776–88
- [42] Barbera G 2009 Theoretical and experimental analysis of a control system for a vehicle biomimetic 'boxfish' *Master Thesis* University of Padua, Padua, Italy
- [43] Barbera G, Pi L and Deng X 2011 Attitude control for a pectoral fin actuated bio-inspired robotic fish *IEEE Int. Conf. on Robotics and Automation (ICRA) (Shanghai, China)* pp 526–31
- [44] Wang J and Tan X 2013 A dynamic model for tail-actuated robotic fish with drag coefficient adaptation *Mechatronics* **23** 659–68
- [45] Fossen T I 1994 *Guidance and Control of Ocean Vehicles* 1st edn (New York: Wiley)
- [46] Bainbridge R 1958 The speed of swimming of fish as related to size and to the frequency and amplitude of the tail beat *J. Exp. Biol.* **35** 109–33
- [47] Banerjee A and Nagarajan S 1997 Efficient simulation of large overall motion of beams undergoing large deflection *Multibody Syst. Dyn.* **113**–26
- [48] Quinn D B, Lauder G V and Smits A J 2015 Maximizing the efficiency of a flexible propulsor using experimental optimization *J. Fluid Mech.* **430**–48
- [49] Quinn D B, Lauder G V and Smits A J 2014 Scaling the propulsive performance of heaving flexible panels *J. Fluid Mech.* **738** 250–67
- [50] Alben S, Witt C, Baker T V, Anderson E and Lauder G V 2012 Dynamics of freely swimming flexible foils *Phys. Fluids* **24** 051901
- [51] Michelin S and Llewellyn Smith S G 2009 Resonance and propulsion performance of a heaving flexible wing *Phys. Fluids* **21** 071902